Northumbria Research Link

DEVELOPMENT OF A WORKFLOW

FOR PROCESSING GPR DATA FROM MULTI-CONCURRENT RECEIVERS

Dimitrios Angelis[1][*], Craig Warren[1], Nectaria Diamanti[2], James Martin[1] and A. Peter Annan[3]

Right Running Head: MULTI-OFFSET GPR DATA PROCESSING

[*] Corresponding author

[1] Department of Mechanical and Construction Engineering, Northumbria University, Newcastle upon Tyne, NE1 8ST, United Kingdom. E-mail: dimitrios.angelis@northumbria.ac.uk; craig.warren@northumbria.ac.uk; james.e.martin@northumbria.ac.uk

[2] Department of Geophysics, Aristotle University of Thessaloniki, Thessaloniki, 541 24, Greece. E-mail: ndiamant@geo.auth.gr

[3] Sensors & Software Inc., 1040 Stacey Court, Mississauga, L4W 2X8, ON, Canada. E-mail: peter.annan@spx.com

ABSTRACT

Ground Penetrating Radar (GPR) systems with multi-concurrent sampling receivers can rapidly acquire dense multi-offset GPR data, which is not feasible using typical common offset (CO) GPR systems with a single, fixed offset transmitter-receiver pair. Multi-offset GPR data from these new multi-concurrent receiver systems have the potential to be used to create detailed subsurface velocity models and enhanced reflection sections. These are important features that can improve qualitative and quantitative interpretation of GPR data. In order to realize these benefits and to deal with the large amount of multi-offset data generated by these new systems, we have developed an automated and customized data processing workflow. There are three key algorithms that we have developed as part of our workflow, which are crucial for processing large volume, multi-offset GPR data so as: firstly, to efficiently correct and manage time misalignments from multi-concurrent receivers; secondly, to carry out trace balancing of common mid-point (CMP) data for semblance analysis; and thirdly, to automate the velocity analysis step. We showcase our processing workflow using two field datasets acquired using a multi-concurrent sampling receiver GPR system consisting of one transmitter and seven receivers. The field data were collected at two different locations: a site using a system with a 500 MHz center frequency and another site using a system with a 1000 MHz center frequency. We demonstrated, with both datasets, that our processing workflow could produce automated stacking velocity fields and enhanced zero-offset reflection cross-sections. These benefits increase the information that can be used for interpretation (compared to conventional CO data) and can form the basis of further processing steps such as migration. As the cost of these multi-concurrent sampling receiver systems decreases over time, we anticipate their use, and the acquisition of dense multi-offset GPR data, to become much more commonplace.

INTRODUCTION

Ground Penetrating Radar (GPR) is an active, high frequency (2 MHz – 2 GHz) electromagnetic (EM) geophysical technique that exploits the wave character of EM fields and is used to detect dielectric discontinuities in the shallow subsurface (typically < 50 m) (Neal, 2004). GPR is non-destructive and can generally provide very fast, high-resolution data as well as on-site feedback (Annan, 2005). For these reasons, it is used either as a standalone technique or in combination with other methods for a wide range of near-surface applications, such as archaeological (Angelis et al., 2018), geological (Rashed et al., 2003), environmental (Endres et al., 2000), engineering (Diamanti et al., 2017), and security (Diamanti and Annan, 2019).

GPR data can be collected from the surface using a variety of different survey methods, as illustrated in Figure 1. The most frequently used acquisition mode is the single-fold (SF) common offset (CO), which operates with a single transmitter (Tx) and receiver (Rx) pair moving along the survey line while maintaining a constant separation distance (offset). The main advantage of this mode of operation is that it allows rapid and dense data acquisition and therefore, high-resolution, large-scale investigations to be carried out with relative ease and at a relatively low cost. There are also multi-fold (MF) acquisition modes such as the common mid-point (CMP) and the wide-angle reflection-refraction (WARR). For CMP, both the Tx and Rx are moved simultaneously away from a fixed location, whilst in WARR mode the Tx or Rx remains at a fixed position whilst the other is moved along the survey line at regular intervals.
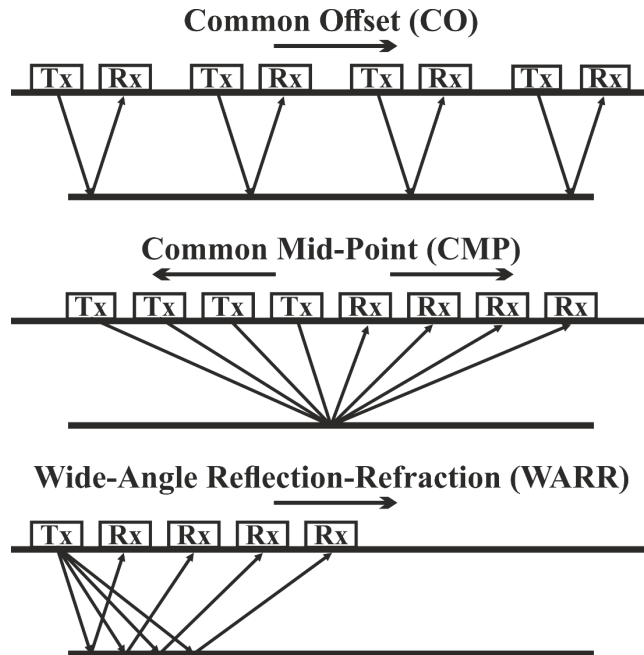
Figure 1. GPR data acquisition modes.

MF GPR modes have many advantages over the SF CO mode, as they allow each subsurface point to be mapped through multiple Tx-Rx pairs, and thus, through multiple wavefronts (Forte and Pipan, 2017). The advantages of MF GPR modes have been described and demonstrated over the years by many researchers (Annan and Davis, 1976; Fisher et al., 1992; Macheret et al., 1993; Greaves et al., 1996; Pipan et al., 1999; Murray et al., 2000, 2007; Nakashima et al., 2001; Bangbing et al., 2006; Bradford, 2006; Berard and Maillol, 2007; Bradford et al., 2009; Booth et al., 2010; De Domenico et al., 2013; Forte and Pipan, 2017), with the most important being:

- the ability to provide detailed subsurface EM wave velocity models and thus, additional models of other subsurface properties using mixing equations (Topp et al., 1980; Endres et al., 2009);

- the ability to provide enhanced reflection sections with a higher signal-to-noise ratio (SNR) and hence, improved exploration depth, reflection continuity as well as dip imaging;

- the potential to process GPR data in a similar way to seismic reflection data due to the similarities of the two respective wave fields (Ursin, 1983; Carcione and Cavallini, 1995) and therefore, the possibility to exploit many of the advanced processing schemes of the latter, which are already developed and well-established.

Despite the many advantages of MF GPR data acquisition modes, they have seen limited adoption in recent decades. This is because they are not suitable for all environments, e.g., high moisture settings without distinct reflectors, and most importantly, these acquisition modes have typically required significantly more survey time and consequently, increased costs compared with CO. However, recent advances in GPR hardware, particularly in timing and control technology, have enabled the development of multi-channel GPR systems with multiple concurrent data acquisition receivers such as the "WARR Machine", shown in Figure 2 and manufactured by Sensors & Software Inc. (Annan and Jackson, 2017; Diamanti et al., 2018). These systems are able to carry out simultaneous sampling from all receivers rather than the multiplexed sampling that is typical in multi-channel array GPR systems that collect multiple CO data (Trinks et al., 2018). Multi-concurrent sampling receiver GPR systems have the potential to provide all the aforementioned benefits with considerably less effort and therefore, reduced survey cost, as they allow for the fast acquisition of multi-offset WARR soundings (e.g., the

"WARR Machine" allows for the simultaneous, multi-concurrent, acquisition of up to seven CO

profiles which can be sorted into WARRs or CMPs) at the same speed as CO mode of operation.

Nevertheless, such systems can generate thousands of WARR/CMP gathers per hour, all

of which can potentially be analyzed and contribute to the purpose of a survey. Although the

acquisition and processing of such large volumes of multi-offset data is typical in reflection

seismics, it has not been commonly done for GPR surveys. Therefore, it becomes understandable

that the development of a systematic processing procedure as well as automation in processing,

are required. Moreover, despite similarities between GPR and seismic reflection data, there are

also significant differences, for example with time-zero alignment, amplitude versus offset

(AVO) attenuation, and velocity. Such differences require the adaption or development of new

processing algorithms (Diamanti et al., 2018; Kaufmann et al., 2020).

Figure 2. Sensors & Software Inc., "WARR Machine".

In this paper, following the preliminary work conducted by Angelis et al. (2019), we develop a comprehensive processing workflow for dense, multi-offset GPR data acquired from multi-concurrent sampling receiver systems. The paper begins with a description of the field data used to demonstrate our processing workflow, which were acquired using a multi-concurrent sampling receiver GPR system with one transmitter and seven receivers. We then present our comprehensive processing workflow and describe in detail three new approaches that we have developed to address challenges with dense multi-offset GPR data, namely timing alignment, CMP balancing in the presence of strong AVO attenuation, and automation of velocity analysis. Finally, we use the complete data processing workflow to produce detailed stacking velocity cross-sections, as well as enhanced zero-offset reflection time sections.

DATA ACQUISITION

The field data were collected using the Sensors & Software Inc. "WARR Machine" (Diamanti et al., 2018), which is a multi-concurrent receiver GPR system with one transmitter and seven receivers. The transducers were of 500 MHz center frequency, configured in a line, and were separated by 0.25 m (Figure 2). The field site contained a target of interest which was a linear pipe that crossed an asphalt-covered parking lot (white arrow in Figure 3a). The data were collected at a normal walking speed with 16 vertical stacks per trace per receiver and with a constant spatial step of 0.0625 m (i.e., Tx-Rx$_1$ / 4) to allow direct CMP sorting without the need for resampling in distance. The time window and sampling interval were 40 ns and 0.2 ns, respectively. Using the above-reported survey parameters, a ~28 m long transect with seven different offset profiles (equivalent to a total of 461 WARR soundings) was acquired in under 2 minutes. The quality of the collected data can be seen in Figure 3b to Figure 3d which illustrate the CO profile of the first, fourth, and seventh receiver, respectively. For visualization purposes (i.e., to highlight the different subsurface features), both dc-shift removal and an inverse amplitude decay (IAD) gain have been applied to the data. The color scale has also been adjusted accordingly. Clear time misalignments (e.g., the direct air-wave responses of Rx$_7$ and Rx$_4$ are earlier in time than Rx$_1$, despite the increase of the offset – white dotted lines), as well as very strong AVO attenuation (see the amplitude values in the color scales), can be seen in the data.
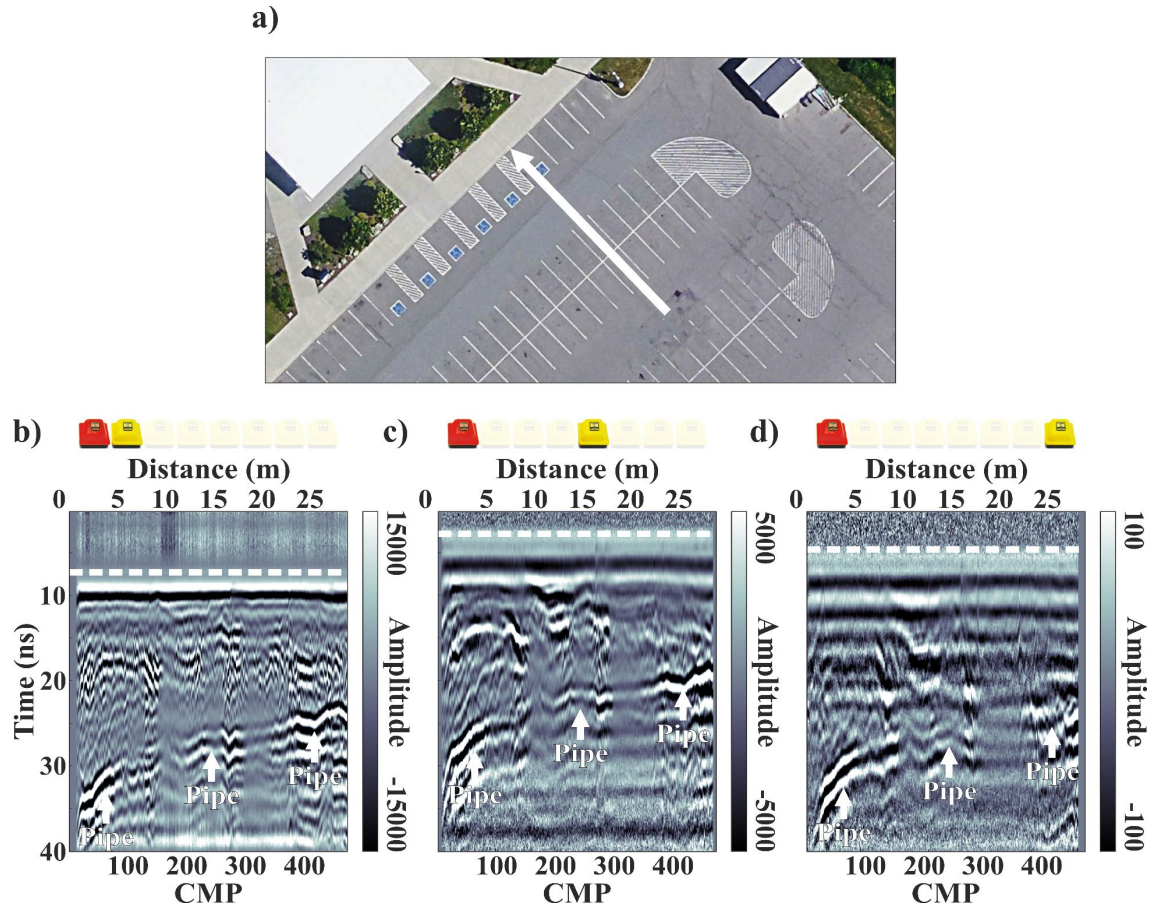
Figure 3. a) Map of the field test site. b) CO profile of the first receiver, Tx-Rx$_1$: 0.25 m. c) CO profile of the fourth receiver, Tx-Rx$_4$: 1.0 m. d) CO profile of the seventh receiver, Tx-Rx$_7$: 1.75 m. In (a) the white arrow indicates the investigated transect, and in (b) – (d) white arrows highlight the linear pipe response. In (b) – (d) the white dotted line highlights the direct air-wave response. At the top of each sub-figure the transducer configuration can be seen, with the Tx depicted in red, and the Rxs in yellow.

DATA PROCESSING

Processing of GPR data is essential, as it can amplify recorded signals, reduce noise, and therefore, highlight subsurface information. Processing is also unavoidable in the case of MF data since special steps are required, some of which have been adopted and/or adapted from well-established seismic data processing methods, to extract detailed subsurface EM wave velocity models, as well as to further boost the SNR. For this work, all processing steps were performed in MATLAB using a software toolset with a graphical user interface (GUI) (Angelis et al., 2020) and are illustrated in Figure 4. The workflow consists of three different sections:

- a section that incorporates common GPR processing steps, i.e., used for CO data (Annan, 2003);

- a section which includes standard seismic processing routines (Yilmaz, 2001; Reynolds, 2011), which have been adapted for GPR;

- a section that incorporates steps to enable the transition of data from the CO to the CMP domain (i.e., CMP gather sort, and if necessary, resampling in distance to correct the spatial trace step to then perform CMP gather sort), as well as other steps necessary to address the aforementioned challenges (i.e., time-zero alignment, CMP trace balancing) and to improve semblance analysis and horizontal stacking (i.e., resampling in time to increase the number of samples, and mute).
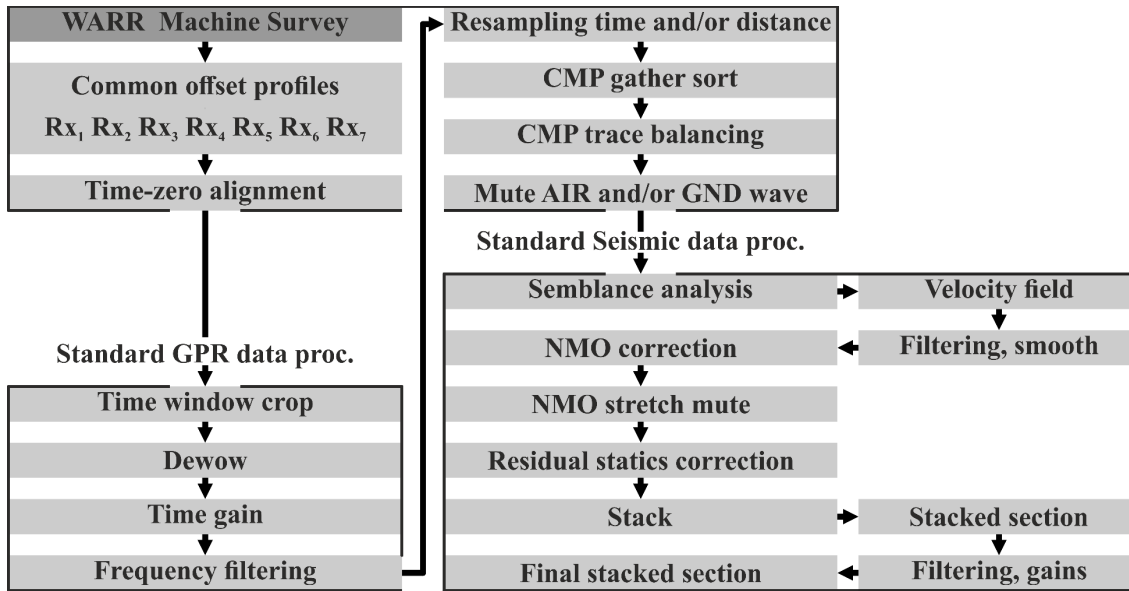
Figure 4. Processing workflow for multi-concurrent sampling receiver GPR data.

Time-zero alignment

Developments in recent decades, in both the hardware (e.g., fiber-optic cables, improved shielding materials) as well as in the interior layout of GPR systems (e.g., cable alignment and positioning, static and stable cables) have allowed for a significant reduction of undesired noise and of drifting time delays (Babcock et al., 2016; Annan and Jackson, 2017). Yet, despite these advances, GPR signals are still affected by various factors such as temperature, supply voltage, cable length, component aging (Sensors & Software Inc., 2001), which can all cause an imperfect synchronization between transmitting and receiving antennas (i.e., a misalignment of the GPR signal in time). With a typical single-channel GPR system consisting of a single Tx-Rx pair, this issue is manageable and addressed with a single time-zero correction (Yelf, 2004). However, as the number of interconnected transducers increases in a system (as in the case of the multi-concurrent receiver system namely the "WARR Machine"), so does the number of corrections required. This is because each receiver requires a unique time correction that is not related to its offset (Figure 5), and is due to the aforementioned factors. In addition, these correction(s) become very challenging to consistently apply for far offset receivers/traces due to their almost indistinguishable direct air-wave responses (a result of pulse dispersion), SNR reduction, and strong AVO attenuation.

The time-zero alignment is the process where each CO profile or each trace in a WARR gather of the corresponding receiver is adjusted so that its first break coincides with the theoretical travel time of the direct air-wave response t_a (i.e., due to the respective Tx-Rx offset – green line in Figure 5) which is given by

$$t_a = \frac{x}{c} \qquad\qquad (1)$$

where, x is the Tx-Rx offset, and c is the velocity of light in free space.

The time-zero alignment is extremely important for NMO based velocity analysis and horizontal stacking, as not doing so will lead to misaligned reflected events in the WARR and CMP domains, and consequently, to false stacking velocity estimations and poor stacking results. Currently, three different methods have been proposed to perform the time-zero alignment process: Diamanti et al. (2018) used air-controlled data from which they estimated the first breaks using an amplitude threshold value on the traces of the respective receivers; Angelis et al. (2019) estimated the first breaks directly from survey data using an amplitude threshold value on enhanced stacked traces of the corresponding receivers; Kaufmann et al. (2020) estimated time misalignments relative to the first receiver by comparing the same dataset obtained for all seven receivers in all positions of the "WARR Machine" sled (i.e., seven WARR gathers, one for each Rx) at one specific location. After repeating this process several times and at different locations, they found that the time misalignments remained consistent. The methods proposed by Diamanti et al. (2018) and Angelis et al. (2019) are disadvantageous as the position of the first breaks from every receiver are difficult to reliably pick (especially in the case of the ground-coupled survey data). The method used by Kaufmann et al. (2020) is time-consuming (~40 minutes) and will likely have to be repeated relatively frequently as the time misalignments will change over the lifespan of the system for the reasons stated above e.g., cable stability, component replacement and/or aging, etc.

We propose a different method for dealing with the time misalignments in multi-

concurrent GPR receivers, which is illustrated in Figure 5. Our method is similar to Diamanti et

al. (2018) as we also use air-controlled data (Figure 5a) because the direct air-waves by

themselves are free from any interference from the direct ground wave. In addition, air-

controlled data have the advantage that they can be collected quickly and easily (i.e., turn the

system upside-down and collect traces in the air). However, rather than realigning the signals

based on estimated positions of first breaks, we use the first peaks or troughs (blue line in Figure

5a), as they can be easily detected (either manually or automatically) and are very stable for the

reason stated above. After the correction of relative time misalignments is completed, a

common-to-all traces, positive static time shift based on the first break of the first receiver (red

dot in Figure 5a) is applied. Although at first glance this process may seem relatively complex,

one can easily realize that the total time shift/correction $t_{shift(Rx_n)}$ required for each CO profile,

or each trace in a WARR gather of the corresponding receiver can be calculated by

$$t_{shift(Rx_n)} = t_{a(Rx_n)} - t_{fpeak(Rx_n)} + t_{fpeak(Rx_1)} - t_{fbreak(Rx_1)} \qquad (2)$$

where, $t_{a(Rx_n)}$ is the theoretical travel time of the direct air-wave for receiver n that can be

calculated by equation 1, $t_{fpeak(Rx_n)}$ is the two way travel time of the first peak of receiver n,

$t_{fpeak(Rx_1)}$ is the two way travel time of the first peak of the first receiver, and $t_{fbreak(Rx_1)}$ is the

two way travel time of the first break of the first receiver. The same time shifts/corrections which

are determined from the air-controlled data can then be applied to the field data as shown in
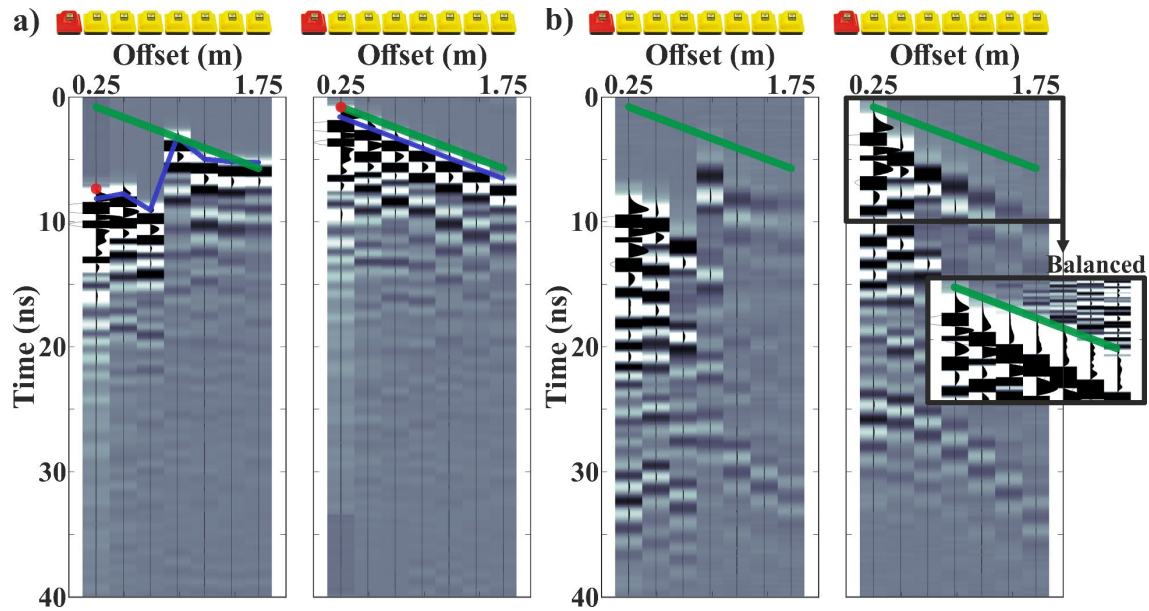
Figure 5b.

Figure 5. a) Air-controlled data WARR gather before and after time-zero alignment. The necessary time shift/correction for each trace has been calculated using equation 2. b) Field data WARR gather before and after time-zero alignment. The necessary time shift/correction for each trace has been calculated from the air-controlled data of (a). To aid visualization, the first 10 ns are also shown after trace balancing. In (a) the blue line highlights the first peaks, and the red dot the first break of the first receiver. In (a) and (b) green line highlights the theoretical direct air-wave response which is given by equation 1. At the top of each sub-figure the transducer configuration can be seen, with the Tx depicted in red, and the Rxs in yellow.

CMP trace balancing

The most common method in GPR for determining stacking velocities, i.e., velocities that allow for optimal horizontal stacking (Mayne, 1962) and which can also under certain conditions (Yilmaz, 2001) be translated into true material velocities (Dix, 1955), is the CMP NMO based velocity analysis using spectra panels (Greaves et al., 1996; Pipan et al., 1999; Nakashima et al., 2001; Berard and Maillol, 2007; Murray et al., 2007; Booth et al., 2010; van der Kruk et al., 2010; De Domenico et al., 2013; Dal Bo et al., 2019; Church et al., 2020; Kaufmann et al., 2020). The velocity spectrum is shown as a plane/panel of velocity versus two-way travel time in which the resultant stacked traces of an NMO corrected CMP gather for a range of constant velocities are plotted side by side (Taner and Koehler, 1969). The desired stacking velocities are obtained by picking the peaks/maxima of the spectra panel that correspond to hyperbolic events of the CMP gather.

Velocity spectra can be calculated using a variety of coherency measures (Yilmaz, 2001). The most widely used in both GPR and seismic reflection methods, due to its simplicity, computation efficiency, as well as robustness against noise (Zhou, 2014), is the normalized output-to-input energy ratio (NE), commonly referred to in the literature as semblance (Neidell and Taner, 1971). Conventional semblance, however, despite its advantages has a major drawback – it does not handle strong AVO variations properly as it assumes constant amplitude models (Sarkar et al., 2001), and consequently, can perform poorly for CMP gather events that are characterized by such variations. Although there is a coherency measure known as AB semblance (Sarkar et al., 2002) which was developed specifically to handle AVO, it is more

computationally expensive, twice as sensitive to noise, and has half the resolution of its

conventional counterpart (Fomel, 2009).

As previously shown in Figure 3, MF GPR data can suffer from strong AVO attenuation.

Therefore, apart from the standard time-variant amplitude scaling (i.e., the application of a time

gain function), some additional scaling is required for the GPR CMP gather traces to compensate

for the large, and in some cases extreme, AVO differences. Such balance is essential for an

effective velocity/semblance analysis, as it can potentially improve the resolution of the

semblance panel/plot, i.e., the sharpness as well as strength of the peaks corresponding to

hyperbolic events, and thus, the velocity information obtained. Furthermore, the additional

scaling could also be beneficial to horizontal stacking, since, with such strong attenuation as that

illustrated in the example above, the contribution of the far offset traces to the stack can be

minimal to nonexistent.

For this purpose, a trace balancing scheme often referred to as trace equalization, could

be used. Trace balancing, as described by Yilmaz (2001) is a time-invariant amplitude scaling of

the traces to a common root mean square (RMS) level. More specifically, for each trace in a

group/gather of traces, a single time-invariant balance/scaling factor is determined and applied.

In the most simplistic form, the balance factor is defined as the ratio of the desired RMS, which

can be that of the near offset trace, to the RMS amplitude of the trace to be balanced. However,

since only a single factor is being used for each trace (i.e., the process is analogous to a single-

window AGC), this essentially means that potentially not all events in the CMP gather will be

balanced properly, and especially when there are noise bursts in the traces. Consequently, not all

corresponding semblance responses will be sharp and strong, which in turn can lead to poor

velocity estimates. Therefore, we propose a modified trace balancing with a sliding window, as this enables the determination of not one, but multiple balance factors for each trace. In addition, we add one more step in the process that allows for the use of smaller windows, and hence, for improved balancing.

Figure 6 illustrates, from left to right, the steps of our proposed balancing approach using a field data CMP gather (CMP 45). As can be seen, at first the traces are shifted upwards in time (green arrows left-hand side) using equation 1 so that the first breaks, i.e., the direct air-wave responses (green line), are at the same position in time and appear horizontal. This step aims to reduce the time window in which a hyperbolic event appears in the gather, and hence, to allow the use of a smaller length sliding window for the balancing process that follows. Next, using a sliding tapered window, the length of which is user-defined (10 ns window in the example below), the desired RMS amplitudes are calculated from the first trace, which currently works as a reference trace (red rectangle, and red arrow). Similarly, the RMS amplitudes of the second trace are also calculated (blue rectangle, and blue arrow). The ratio of the aforementioned amplitudes gives the balance factors for the second trace (black rectangle). Then, the balance factors are applied to the second trace (black arrow), and the factors for the third trace are determined, this time using the second and already balanced trace as a reference. The process continues in the same way for the remaining traces in the gather. The use of tapering in the window allows for smoother balancing factors, whereas the moving reference trace scheme is being used to reduce horizontal overbalancing. Lastly, the traces are shifted forward in time (green arrows right-hand side), using equation 1, to their original position.
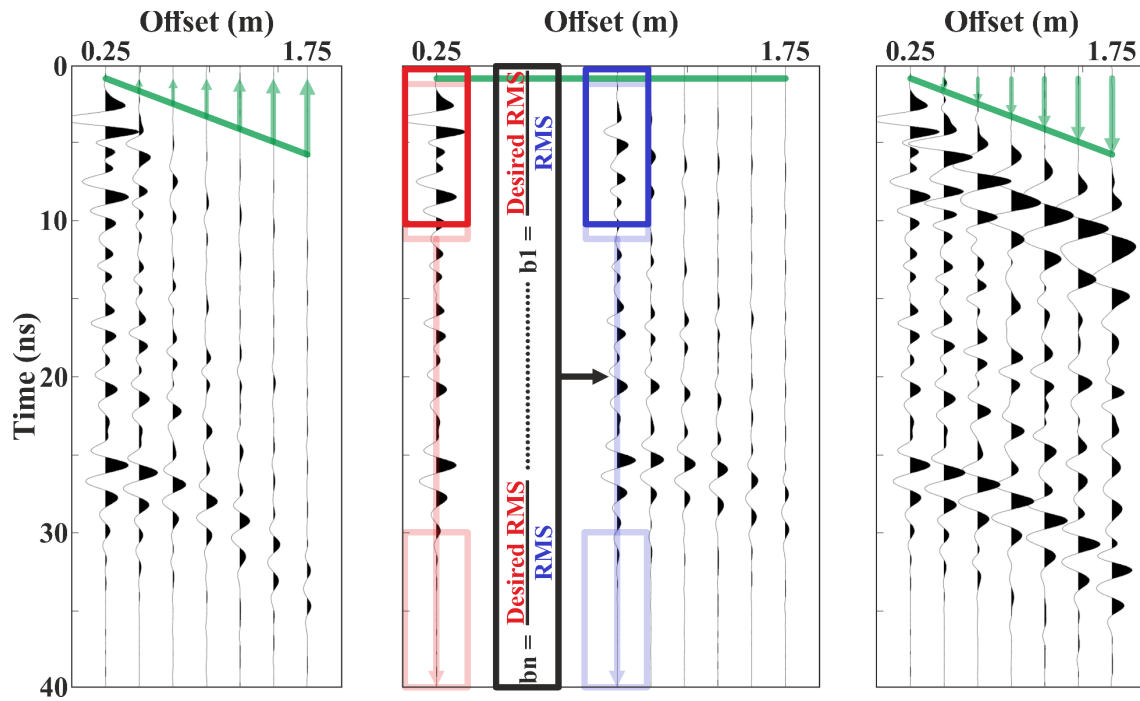
Figure 6. From left to right the stages of the proposed CMP trace balancing approach (field data CMP gather 45). The green line highlights the direct air-wave responses, whereas the green arrows indicate the time shift, to either negative or positive times, which is given by equation 1. The red and blue rectangles highlight the sliding window (10 ns windows) for the first and second trace, respectively, while the black rectangle and arrow indicate the computed balance factors and their application to the second trace.

To demonstrate the importance of CMP trace balancing in semblance analysis, as well as the advantages of our proposed sliding window balancing method over the single-window one, we applied our approach to the field data CMP gathers. We then compared the resultant semblance panels with the corresponding semblance and AB semblance panels computed from the unbalanced CMP gathers as well as from balanced gathers obtained using the typical single-window trace balancing method. In addition, we also compared the semblance curves computed for each case from the time window centered on the pipe response/event. Figure 7a shows two of the unbalanced CMP gathers (CMP 100 and CMP 203) along with their computed semblance plots and semblance curves. As can be seen, the gathers suffer from very strong AVO attenuation and as a result, with the exception of the peak corresponding to the pipe response in the CMP gather 100 (semblance curve in Figure 7a), they produce weak semblance responses. Furthermore, due to the significant AVO differences, the contribution of the far offset traces to the semblance summation is minimal, which potentially means that the stacking velocities extracted from the semblance peaks may not be optimal. The same unbalanced CMP gathers are depicted along with their computed AB semblance plots and curves in Figure 7b. As expected, since the AB measure is designed to handle AVO variations, the AB semblance plots exhibit very strong peaks for most hyperbolic events of the gathers. However, when compared to the conventional semblance plots of Figure 7a, it can be clearly seen that there is a significant reduction in the sharpness of the peaks (i.e., a loss of velocity resolution) which could lead to inaccurate velocity estimates. This is also particularly evident in the corresponding curves. Notice how much stronger but at the same time how much broader the peaks in the AB semblance curves in Figure 7b are compared to the conventional in Figure 7a.

Finally, Figure 7c and Figure 7d show the balanced CMP gathers obtained using the single-window and proposed sliding window trace balancing method, respectively, with their corresponding semblance plots and curves. The first observation is that the resultant balanced gathers from both methods produce stronger semblance responses than those of the unbalanced gathers of Figure 7a and much sharper responses than in the AB semblance panels shown in Figure 7b. However, there is an exception in Figure 7c where the single-window trace balancing method actually further unbalanced the CMP gather 100. This is also reflected in the peak corresponding to the pipe event which is weaker compared to that of Figure 7a. The second and most important observation is that the CMP gathers produced by our proposed method (Figure 7d) are significantly better balanced than those of the single-window method (Figure 7c). This alone can potentially improve the stacking results which is also reflected in the corresponding semblance panels and semblance curves that exhibit stronger and slightly sharper peaks. These results illustrate both the importance of CMP trace balancing in semblance analysis, as well as the performance of our proposed method. However, it should be also noted that with the application of any such trace balancing method the relative amplitude information is lost. Therefore, such balancing should only be performed for velocity analysis if the objective of the research/survey is the interpretation of the AVO changes.
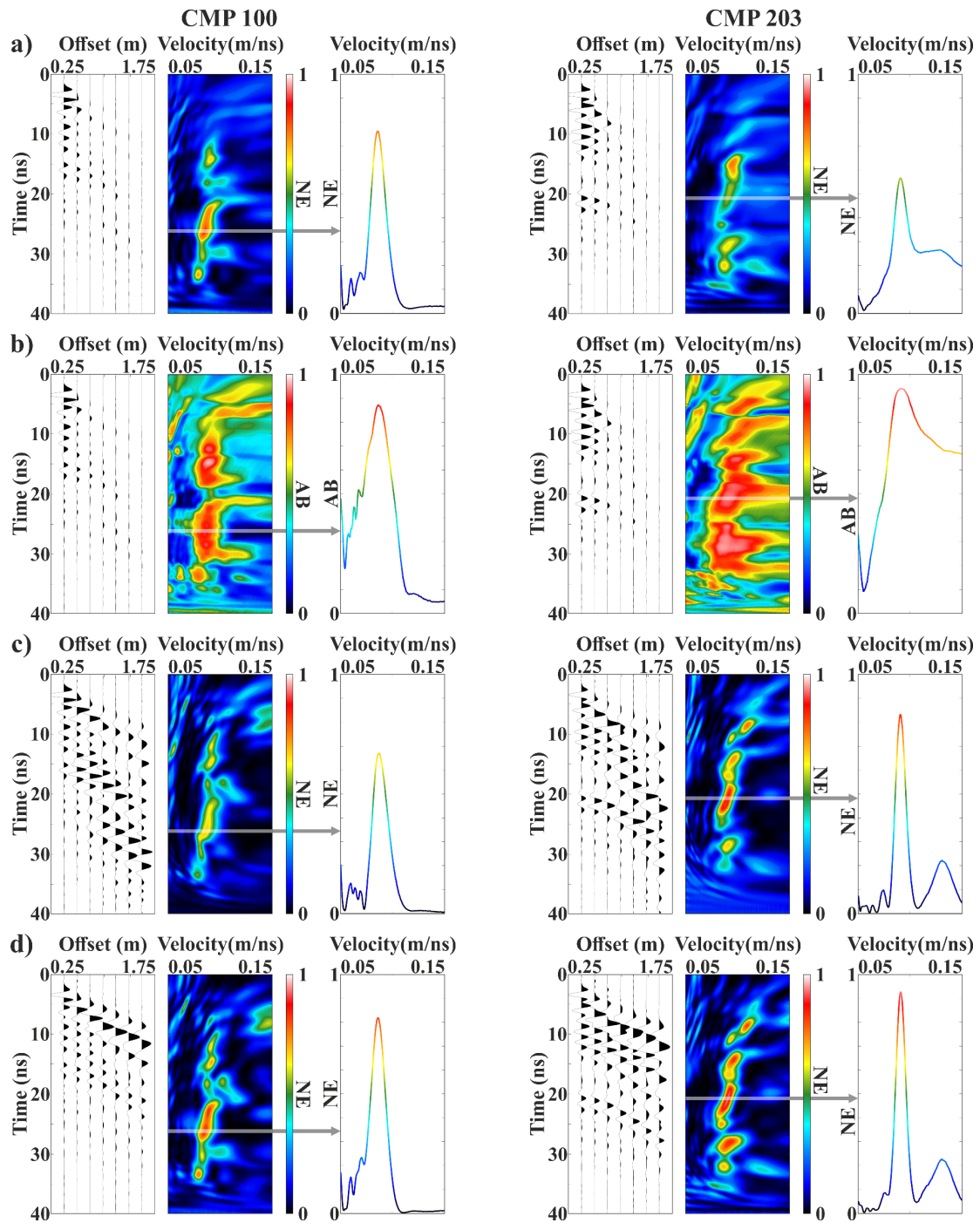
Figure 7. a) Unbalanced CMP gathers and their respective semblance plots. b) Unbalanced CMP gathers and their respective AB semblance plots. c) Balanced CMP gathers using the typical single-window RMS balancing method and their respective semblance plots. d) Balanced CMP gathers using the proposed sliding window RMS balancing method (10 ns window) and their respective semblance plots. In all sub-figures, the semblance or AB semblance curves are from the time window centered on the pipe response/event.

Automatic velocity picking

As previously stated, multi-concurrent sampling receiver GPR systems can generate thousands of WARR/CMP gathers in a timely manner, all of which can potentially be analyzed and contribute to the production of detailed velocity fields, and thus to enhanced subsurface information. Manual velocity picking with such data volumes is extremely time-consuming, therefore, some form of automation is required. While there are several automatic velocity picking algorithms, most of them are computationally intensive and have been primarily developed for handling seismic data semblance panels. These panels generally lack irregularities, as they are usually calculated by CMP gathers with very high stacking fold (sometimes even hundreds of traces), which is known to directly affect the velocity spectra/semblance resolution (Yilmaz, 2001). Consequently, these algorithms are not optimal for handling multi-concurrent sampling receiver GPR semblance data, as unlike seismic, they can be quite irregular and can often contain spurious peaks. This is mainly due to the much smaller stacking fold which in this case solely depends on the total number of Rxs in the GPR system (equal to seven for the "WARR Machine"), as well as due to the character of the GPR data in general which tend to have steep high angle dips and many localized diffraction events. Therefore, to effectively analyze the large volume of CMP data, we developed an algorithm based on work first presented by Fomel (2003), that overcomes these issues. Our algorithm is fully automated and performs in an iterative fashion, a reweighted regularization of velocity picks. In the following, we discuss our algorithm operation in detail using a field data CMP gather (CMP 50) (Figure 8a).

First, we scan the semblance panel at each two-way travel time and pick the velocity where the semblance is maximum (red line in Figure 8b). We then regularize the velocity picks using a small regularization parameter and a weight w which is given by

$$w = w_s * w_v \tag{3}$$

where, w_s is a weight that is associated with the semblance values of the picks, and w_v a weight that is associated with the velocity difference of the picks from the linear trend. The first weight w_s is given by

$$\begin{cases} w_s = s \\ w_s < th_s = 0 \end{cases} \tag{4}$$

where, s is simply the corresponding semblance values of the chosen picks and th_s a user-defined threshold value (0.5 in the example below). This weight ensures that a high semblance velocity pick will not be regularized as much. In addition, it is also used to calculate the weighted linear fitted curve of the picks (blue line in Figure 8b). The second weight w_v is defined as

$$\begin{cases} w_v = 1 - \left(\dfrac{|v_d|}{th_v} \right) \\ w_v < 0 = 0 \end{cases} \qquad (5)$$

where, v_d is the absolute velocity difference of the picks (red line in Figure 8b) and the fitted

curve (blue line in Figure 8b), and th_v is a user-defined value (0.05 in the example below) which

is used to normalize the velocity difference. This weight ensures that even high semblance picks

that are far from the trend and could potentially be spurious, will be regularized as much as

possible (white arrows in Figure 8d). Finally, the resultant regularized velocity picks of the first

iteration (white line in Figure 8b) are used as preset picks for the second iteration (red line in

Figure 8c). The process continues in the same way for a number of user-defined iterations or

until the RMS percentage difference of the current and regularized velocity function is very

small (Figure 8d).
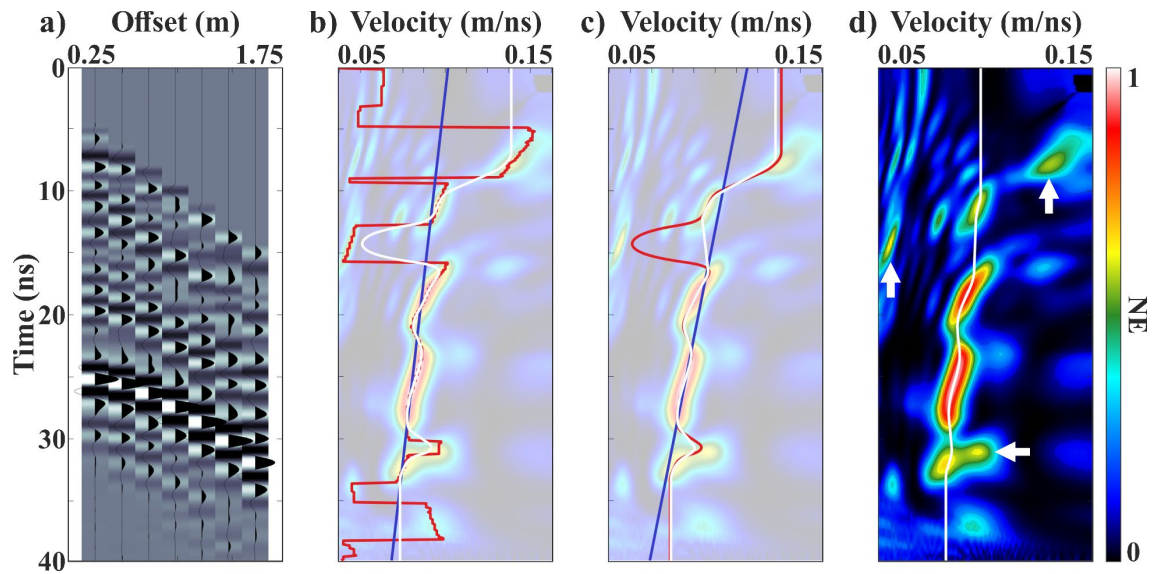
Figure 8. a) Field data CMP gather (CMP 50). b) Semblance plot of (a) the automatic velocity picks during the first iteration. The red line highlights the initial automatic velocity picks based on the semblance maxima at each two-way travel time, the blue line indicates the weighted fit curve of the initial picks, and the white line shows the regularized velocity picks. c) Semblance plot of (a) the automatic velocity picks at the second iteration. The red line highlights the regularized velocity picks of the previous iteration (i.e., white line in (b)), the blue line indicates the new weighted fit curve of those picks, and the white line shows the new regularized velocity picks. d) Semblance plot of (a) the automatic velocity picks at the final iteration. The white line highlights the regularized velocity picks, and the white arrows show spurious peaks that were not picked by the algorithm. To aid visualization in (b) and (c) the transparency of the semblance plot has been adjusted.

VELOCITY FIELD AND STACKED SECTION

In addition to addressing the main challenges of processing multi-concurrent receiver GPR data, the primary objective of this work is to establish and use a processing workflow (Figure 4) in order to automatically extract detailed stacking velocity fields that can subsequently be used to produce enhanced stacked reflection sections. To achieve this objective, we tested our automatic velocity picking algorithm on field data. Although according to the literature velocity analysis is usually performed on a selected number of CMP gathers, typically with high SNR, we chose to perform the analysis in all the field data gathers. We made this decision as we wanted to test our algorithm, and because the field data had a clear and slightly dipping event (response from a pipe) across the whole survey line, as can be observed in the CO profile of the first receiver (Figure 9a).

Figure 9b shows the resultant stacking velocity cross-section obtained through the automated analysis. Since the analysis was performed on all gathers, no interpolation was necessary. To remove velocity outliers, and consequently create a more accurate and suitable velocity field for the stacking process, we took advantage of the high volume of data and applied to the field alpha-trimmed mean filtering every seventh 1D velocity function (i.e., every ~0.45 m) and 2D Gaussian smoothing using a kernel with a standard deviation of 2 (i.e., ~0.5 % the size of the field). Although we could further filter/smooth the velocity field, we chose not to as we only wanted to eliminate the extreme outliers, while preserving at the same time as much as possible the general local velocity variations, as these could potentially be related to real local changes in material properties. The filtered velocity field is shown in Figure 9c.

Subsequently, we used this velocity section to stack the CMP gathers and create an NMO corrected, zero-offset, stacked section, which is illustrated in Figure 9d. By comparing the CO profile (Figure 9a) with the stacked section (Figure 9d), the first thing that is immediately observed is that there is a change in the frequency content, and in particular, a general shift to lower frequencies, as well as a slight decrease in the vertical resolution. These effects are expected and are a consequence of the horizontal stacking of NMO corrected and therefore, stretched CMP gathers, when the wavelets are not perfectly constant and horizontal (Forte and Pipan, 2017). The second thing that is observed is that there is a significant reduction of the high-frequency noise, as well as a slight decrease of the ringing noise that is caused by the reverberation of the GPR wave in the pipe (e.g., the area indicated with a red arrow). Finally, it is observed that there is an improved reflector continuity in many areas (e.g., the reflector marked with a blue arrow) and that reflectors that previously were not clearly visible, have now been significantly enhanced (e.g., the reflector highlighted with a white arrow). These results not only validate the obtained velocity field but also our automated velocity picking algorithm.
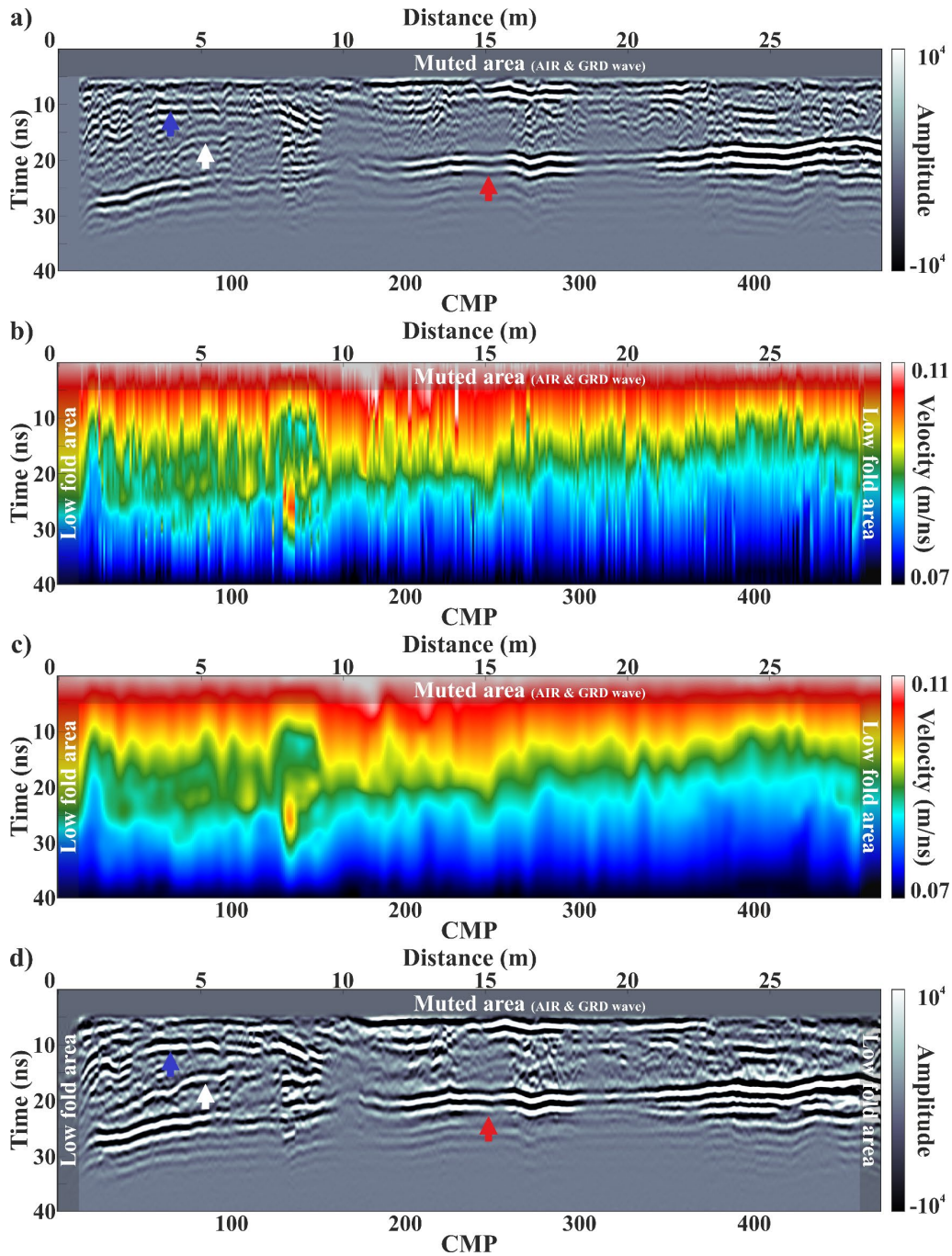
Figure 9. A 500 MHz center frequency "WARR Machine" dataset. a) Processed CO profile of the first receiver. b) Stacking velocity field derived through automated velocity analysis. c) Filtered and smoothed stacking velocity field of (b). d) NMO corrected, zero-offset, stacked section, obtained using the velocity field of (c). In (a) and (d) the red arrow indicates an area with reduced ringing noise, the blue arrow marks a reflector with improved continuity, and the white arrow highlights an enhanced reflector. In each sub-figure, the low fold areas and the muted area of the direct air and direct ground wave are also highlighted.

DISCUSSION

Our main aim was to investigate NMO based velocity analysis and horizontal stacking for multi-concurrent sampling receiver GPR data (i.e., essentially large volume, low fold GPR data with strong AVO attenuation and time misalignments), in order to obtain automated stacking velocity cross-sections as well as enhanced zero-offset reflection sections. We have shown that this is possible by using a workflow consisting of processing steps developed solely to address the key challenges associated with this type of data, along with other standard GPR and seismic reflection data processing steps.

To further evaluate this workflow, we have applied it to a variety of datasets collected from different environments and by different GPR systems with multiple concurrent data acquisition receivers. One such additional dataset is shown in Figure 10 along with the corresponding results (i.e., unfiltered and filtered stacking velocity field and NMO corrected zero-offset stacked section). It should be noted that for this dataset, in contrast to the previous one, a combined linear moveout (LMO) NMO semblance analysis approach was used (Dal Bo et al., 2019; Kaufmann et al., 2020), as there was a very clear and coherent response of the direct ground wave. Field data were collected using the Sensors & Software Inc. "WARR Machine" with 1000 MHz center frequency transducers this time, separated by 0.165 m. The site was a shipping container storage yard that was recently paved with thick asphalt and identified as an ideal location for collecting data with the 1000 MHz center frequency system. The site had just been re-paved and several lifts of asphalt were used to create a very thick asphalt to accommodate heavily loaded trucks. The result is a site with multiple shallow layers that are relatively flat-lying. By comparing the CO profile (Figure 10a) with the stacked section (Figure

10d) all the benefits seen in the previous example/dataset can also be seen here despite the

differences in environment, system, center frequency, etc.

The results from both datasets confirm the efficiency of our processing algorithms and

workflow and demonstrate the true potential of the newly developed GPR systems with multi-

concurrent sampling receivers. However, there are numerous topics that can be explored further.

For example, in this work, we have mainly focused on the production of automated stacking

velocity cross-sections as well as enhanced zero-offset reflection time sections. The application

of prestack time/depth migration techniques along with depth imaging is the next logical step in

this workflow. Moreover, in this work, we took advantage of the high volume of data that can be

generated by these systems to filter out velocity outliers and improve the resultant velocity fields.

Other techniques that can exploit this high volume of data such as super CMP gathers and spatial

semblance filtering could also be used to suppress spurious peaks in the semblance panels and

improve velocity picking. Finally, different transducer configurations such as with two

transmitters and/or with fewer receivers to reduce the cost of such a system could also be

investigated.
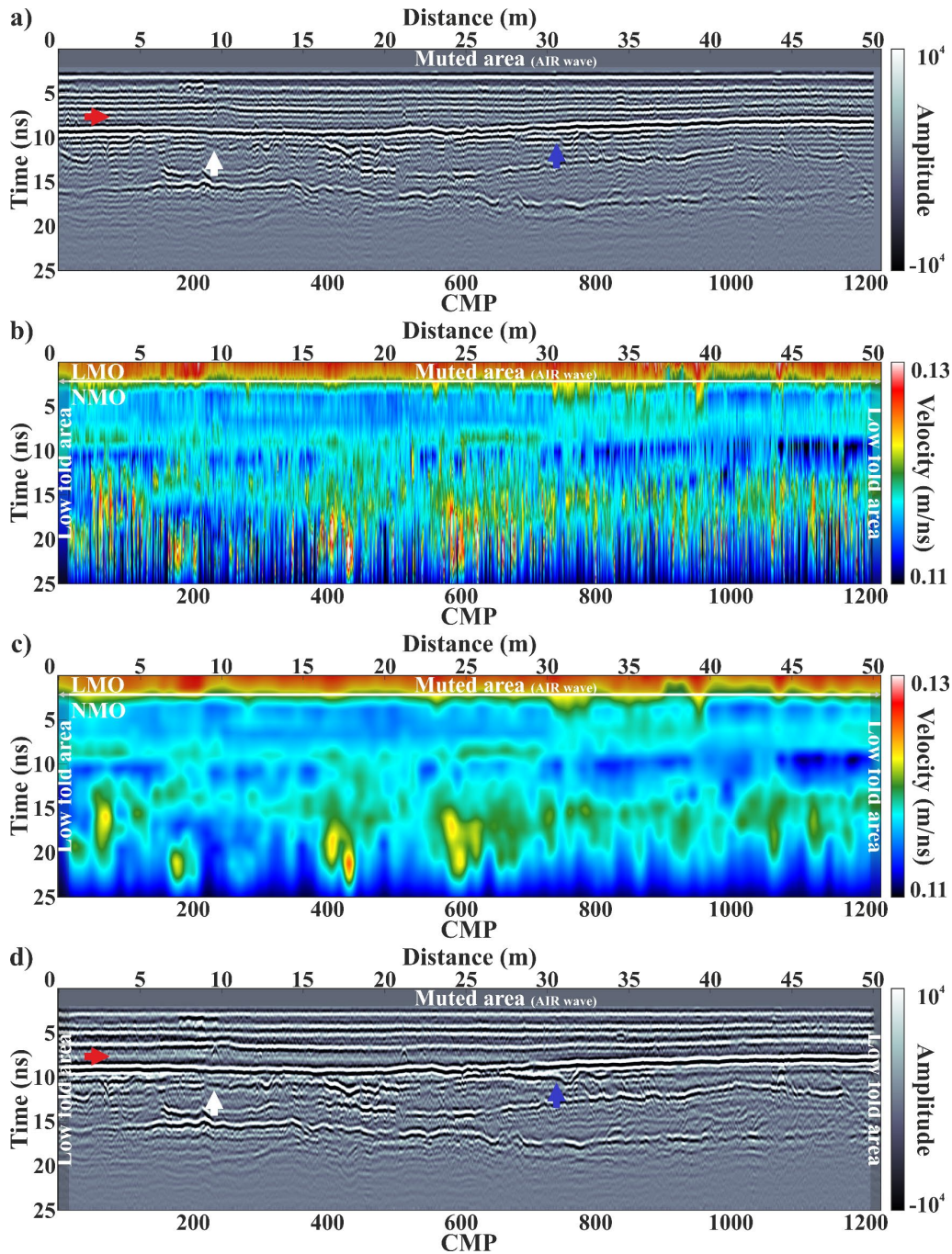
Figure 10. A 1000 MHz center frequency "WARR Machine" dataset. a) Processed CO profile of the first receiver. b) Stacking velocity field derived through automated velocity analysis using a combined LMO NMO semblance analysis. c) Filtered and smoothed stacking velocity field of (b). d) NMO corrected zero-offset stacked section, obtained using the velocity field of (c). In (a) and (d) the red arrow indicates a layer with reduced ringing noise, the blue arrow marks a reflector with improved continuity, and the white arrow highlights an enhanced reflector. In each sub-figure, the low fold areas and the muted area of the direct air-wave are also highlighted.

CONCLUSION

Novel GPR systems with multiple concurrent data acquisition receivers enable rapid acquisition of multi-offset data and offer many benefits including the ability to obtain velocity models and enhanced reflection sections in a timely manner that was not possible before. However, both the character and the large volume of the data generated by these systems necessitates both the development and automation of new processing workflows. We have developed processing algorithms for multi-concurrent sampling receiver GPR data to address three key issues: efficient correction of time misalignments from multiple receiver data, CMP trace balancing for semblance analysis, and generation of automated velocity analysis. Field data from two different environments and two different multi-concurrent sampling receiver GPR systems have been used to demonstrate our processing workflow and produce detailed stacking velocity fields and enhanced zero-offset reflection time sections. The increase in information possible with these systems compared to the conventional CO approach was demonstrated. With the development of new processing workflows for multi-offset GPR data, there are further opportunities to exploit the large volumes of data acquired and to add additional processing steps, such as migration, to the framework.

ACKNOWLEDGEMENTS

REFERENCES

Angelis, D., C. Warren, and N. Diamanti, 2019, Preliminary development of a workflow for
processing multi-concurrent receiver GPR data: 10th International Workshop on Advanced
Ground Penetrating Radar, 1–7.

Angelis, D., C. Warren, and N. Diamanti, 2020, A software toolset for processing and
visualization of single and multi-offset GPR data: 18th International Conference on Ground
Penetrating Radar, Golden, Colorado, 14–19 June 2020, 320–323.

Angelis, D., P. Tsourlos, G. Tsokas, G. Vargemezis, G. Zacharopoulou, and C. Power, 2018,
Combined application of GPR and ERT for the assessment of a wall structure at the
Heptapyrgion fortress (Thessaloniki, Greece): Journal of Applied Geophysics, **152**, 208–
220.

Annan, A. P., 2003, Ground Penetrating Radar: Principles, Procedures & Applications: Sensors
& Software Incorporated.

Annan, A. P., 2005, 11. Ground-Penetrating Radar, *in* Near-Surface Geophysics, , .
Investigations in GeophysicsSociety of Exploration Geophysicists, 357–438.

Annan, A. P., and J. L. Davis, 1976, Impulse radar sounding in permafrost: Radio Science, **11**,
383–394.

Annan, A. P., and S. R. Jackson, 2017, The WARR Machine: 2017 9th International Workshop
on Advanced Ground Penetrating Radar, IWAGPR 2017 - Proceedings, 1–4.

Babcock, E. L., A. P. Annan, and J. H. Bradford, 2016, Cable Effects in Ground-Penetrating
Radar Data and Implications for Quantitative Amplitude Measurements: Journal of
Environmental and Engineering Geophysics, **21**, 99–104.

Bangbing, W., T. Gang, S. Bo, G. Jinxue, and Z. Xiangpei, 2006, An analysis of the multi-fold

    method for GPR exploration: Applied Geophysics, **3**, 187–191.

Berard, B. A., and J. M. Maillol, 2007, Multi-offset ground penetrating radar data for improved

    imaging in areas of lateral complexity - Application at a Native American site: Journal of

    Applied Geophysics, **62**, 167–177.

Booth, A. D., R. A. Clark, K. Hamilton, and T. Murray, 2010, Multi-offset ground penetrating

    radar methods to image buried foundations of a Medieval Town Wall, Great Yarmouth,

    UK: Archaeological Prospection, **17**, 103–116.

Bradford, J. H., 2006, Applying reflection tomography in the postmigration domain to multifold

    ground-penetrating radar data: Geophysics, **71**, K1–K8.

Bradford, J. H., J. Nichols, T. D. Mikesell, and J. T. Harper, 2009, Continuous profiles of

    electromagnetic wave velocity and water content in glaciers: An example from Bench

    Glacier, Alaska, USA: Annals of Glaciology, **50**, 1–9.

Carcione, J. M., and F. Cavallini, 1995, On the acoustic-electromagnetic analogy: Wave Motion,

    21, 149–162.

Church, G., M. Grab, C. Schmelzbach, A. Bauder, and H. Maurer, 2020, Monitoring the seasonal

    changes of an englacial conduit network using repeated ground-penetrating radar

    measurements: Cryosphere, **14**, 3269–3286.

Dal Bo, I., A. Klotzsche, M. Schaller, T. A. Ehlers, M. S. Kaufmann, J. P. Fuentes Espoz, H.

    Vereecken, and J. van der Kruk, 2019, Geophysical imaging of regolith in landscapes along

    a climate and vegetation gradient in the Chilean coastal cordillera: Catena, **180**, 146–159.

Diamanti, N., and A. P. Annan, 2019, Understanding the use of ground-penetrating radar for

assessing clandestine tunnel detection: The Leading Edge, **38**, 453–459.

Diamanti, N., A. P. Annan, and J. D. Redman, 2017, Concrete Bridge Deck Deterioration

Assessment Using Ground Penetrating Radar (GPR): Journal of Environmental and

Engineering Geophysics, **22**, 121–132.

Diamanti, N., E. Judith Elliott, S. R. Jackson, and A. Peter Annan, 2018, The WARR Machine:

System Design, Implementation and Data: Journal of Environmental and Engineering

Geophysics, **23**, 469–487.

Dix, C. H., 1955, Seismic Velocities From Surface Measurements: Geophysics, **20**(1), 68–86.

De Domenico, D., A. Teramo, and D. Campo, 2013, GPR surveys for the characterization of

foundation plinths within a seismic vulnerability analysis: Journal of Geophysics and

Engineering, **10**.

Endres, A. L., W. P. Clement, and D. L. Rudolph, 2000, Ground penetrating radar imaging of an

aquifer during a pumping test: Ground Water, **38**, 566–576.

Endres, A. L., T. Murray, A. D. Booth, and L. J. West, 2009, A new framework for estimating

englacial water content and pore geometry using combined radar and seismic wave

velocities: Geophysical Research Letters, **36**.

Fisher, E., G. A. McMechan, and A. P. Annan, 1992, Acquisition and processing of wide-

aperture ground-penetrating radar data: Geophysics, **57**(3), 495–504.

Fomel, S., 2003, Time-migration velocity analysis by velocity continuation: Geophysics, **68**(5),

1662–1672.

Fomel, S., 2009, Velocity analysis using AB semblance: Geophysical Prospecting, **57**, 311–321.

Forte, E., and M. Pipan, 2017, Review of multi-offset GPR applications: Data acquisition,

processing and analysis: Signal Processing, **132**, 210–220.

Greaves, R. J., D. P. Lesmes, J. M. Lee, and M. N. Toksöz, 1996, Velocity variations and water content estimated from multi-offset, ground-penetrating radar: Geophysics, **61**(3), 683–695.

Kaufmann, M. S., A. Klotzsche, H. Vereecken, and J. van der Kruk, 2020, Simultaneous multichannel multi-offset ground-penetrating radar measurements for soil characterization: Vadose Zone Journal, **19**, e20017.

van der Kruk, J., R. W. Jacob, and H. Vereecken, 2010, Properties of precipitation-induced multilayer surface waveguides derived from inversion of dispersive TE and TM GPR data: Geophysics, **75**, WA263–WA273.

Macheret, Y. Y., M. Y. Moskalevsky, and E. V. Vasilenko, 1993, Velocity of radio waves in glaciers as an indicator of their hydrothermal state, structure and regime: Journal of Glaciology, **39**, 373–384.

Mayne, W. H., 1962, Common reflection point horizontal data stacking techniques: Geophysics, **27**(6), 927–938.

Murray, T., A. D. Booth, and D. M. Rippin, 2007, Water-content of Glacier-ice: Limitations on estimates from velocity analysis of surface ground-penetrating radar surveys: Journal of Environmental and Engineering Geophysics, **12**, 87–99.

Murray, T., G. W. Stuart, M. Fry, N. H. Gamble, and M. D. Crabtree, 2000, Englacial water distribution in a temperate glacier from surface and borehole radar velocity analysis: Journal of Glaciology, **46**, 389–398.

Nakashima, Y., H. Zhou, and M. Sato, 2001, Estimation of groundwater level by GPR in an area with multiple ambiguous reflections: Journal of Applied Geophysics, **47**, 241–249.

Neal, A., 2004, Ground-penetrating radar and its use in sedimentology: Principles, problems and progress: Earth-Science Reviews, **66**, 261–330.

Neidell, N. S., and M. T. Taner, 1971, Semblance and Other Coherency Measures for Multichannel Data: Geophysics, **36**(3), 482–497.

Pipan, M., L. Baradello, E. Forte, A. Prizzon, and I. Finetti, 1999, 2-D and 3-D processing and interpretation of multi-fold ground penetrating radar data: A case history from an archaeological site: Journal of Applied Geophysics, **41**, 271–292.

Rashed, M., D. Kawamura, H. Nemoto, T. Miyata, and K. Nakagawa, 2003, Ground penetrating radar investigations across the Uemachi fault, Osaka, Japan: Journal of Applied Geophysics, **53**, 63–75.

Reynolds, J. M., 2011, An Introduction to Applied and Environmental Geophysics, 2nd ed..: Chichester, West Sussex.

Sarkar, D., J. P. Castagna, and W. J. Lamb, 2001, AVO and velocity analysis: Geophysics, **66**(4), 1284–1293.

Sarkar, D., R. T. Baumel, and K. L. Larner, 2002, Velocity analysis in the presence of amplitude variation: Geophysics, **67**(5), 1664–1672.

Sensors & Software Inc., 2001, Technical Manual 30: Ekko-for-DVL PulseEKKO 100. User's Guide v1.0.: Sensors & Software Inc.

Taner, M. T., and F. Koehler, 1969, Velocity Spectra. Digital Computer Derivation and Applications of Velocity Functions: Geophysics, **34**(6), 859–881.

Topp, G. C., J. L. Davis, and A. P. Annan, 1980, Electromagnetic determination of soil water content: Measurements in coaxial transmission lines: Water Resources Research, **16**, 574–

582.

Trinks, I., A. Hinterleitner, W. Neubauer, E. Nau, K. Löcker, M. Wallner, M. Gabler, R.

Filzwieser, J. Wilding, H. Schiel, V. Jansa, P. Schneidhofer, T. Trausmuth, V. Sandici, D.

Ruß, S. Flöry, J. Kainz, M. Kucera, A. Vonkilch, T. Tencer, L. Gustavsen, M. Kristiansen,

L.-M. Bye-Johansen, C. Tonning, T. Zitz, K. Paasche, T. Gansum, and S. Seren, 2018,

Large-area high-resolution ground-penetrating radar measurements for archaeological

prospection: Archaeological Prospection, **25**, 171–195.

Ursin, B., 1983, Review of Elastic and Electromagnetic Wave Propagation in Horizontally

Layered Media.: Geophysics, **48**(8), 1063–1081.

Yelf, R., 2004, Where is true time zero? Proceedings of the Tenth International Conference

Ground Penetrating Radar, GPR 2004, **1**, 279–282.

Yilmaz, Ö., 2001, Seismic Data Analysis: Society of Exploration Geophysicists.

Zhou, H.-W., 2014, Practical Seismic Data Analysis: Cambridge University Press.

LIST OF FIGURES